

Evidence for direct neutron decay of the isoscalar giant dipole resonances in ^{90}Zr , ^{116}Sn , and ^{208}Pb

M. Hunyadi,* A. M. van den Berg, B. Davids,† M. N. Harakeh, M. A. de Huu, and H. J. Wörtche
Kernfysisch Versneller Instituut, University of Groningen, 9747 AA Groningen, The Netherlands

M. Csatlós, J. Gulyás, A. Krasznahorkay, and D. Sohler
Institute of Nuclear Research of the Hungarian Academy of Sciences, H-4001 Debrecen, Hungary

U. Garg
University of Notre Dame, Notre Dame, Indiana 46556, USA

M. Fujiwara
Research Center for Nuclear Physics, Osaka University, Mihogaoka 10-1, Ibaraki, 567-0047 Osaka, Japan

N. Blasi
INFN, Milano I-20133, Italy
 (Received 19 October 2006; published 30 January 2007)

The direct and statistical neutron decay of the isoscalar giant dipole resonance was studied in ^{90}Zr , ^{116}Sn , and ^{208}Pb using the $(\alpha, \alpha'n)$ reaction at a bombarding energy of 200 MeV. The spectra of fast decay neutrons populating valence hole-states of the $Z, N - 1$ nuclei were analyzed, and estimates for the branching ratios were determined. The results were compared to recent continuum random-phase approximation calculations.

DOI: [10.1103/PhysRevC.75.014606](https://doi.org/10.1103/PhysRevC.75.014606)

PACS number(s): 24.30.Cz, 25.55.Ci, 27.60.+j, 27.80.+w

I. INTRODUCTION

A systematic investigation of giant resonances and their decay properties is of special importance for a better understanding of how the microscopic structure of nuclei evolves to collective behavior. In a microscopic picture giant resonances are highly coherent one-particle-one-hole (1p-1h) excitations that exhaust major fractions of their energy-weighted sum rules (EWSR). The initial collective configuration of 1p-1h excitations acquire width through fragmentation of the particle-hole energy, the so-called Landau damping, through coupling to the continuum, resulting in direct decay (escape width), and through coupling to 2p-2h excitations and more complicated np-nh configurations (spreading width) as a result of internal collisions. Macroscopically the last of these processes can be viewed as a damping of the collective oscillation state ending up in a thermally equilibrated state of a compound nucleus [1].

Because most of the giant resonances are located above the particle separation thresholds, particle emission is the dominant decay process that can take place at different stages of the damping process. The particle decay can occur either from the initial 1p-1h state, leaving a single-hole state in the $A - 1$ nucleus (direct component), or from the states with partially or completely equilibrated configurations, resulting in an evaporation-like spectrum of the emitted particles

(statistical component). The observation of particle emission spectra following the excitation of giant resonances and the determination of the branching ratios thus provide information on the evolution of the decaying configuration and on the microscopic structure of the giant resonance.

In the last decades, a series of systematic experimental studies focused on the particle decay of isoscalar giant resonances, especially of $E0$ and $E2$ modes [isoscalar giant monopole resonance (ISGMR) and isoscalar giant quadrupole resonance (ISGQR)] excited mostly in inelastic α -scattering experiments [2–9]. In light nuclei, a large fraction of the particle decay of the rather fragmented giant resonances was found to proceed through the direct component. In medium-heavy and heavy nuclei, the observation of significant direct particle decay and its separation from the statistical component has always been a challenging experimental task. For heavy nuclei, charged-particle emission of both the ISGMR and ISGQR is strongly suppressed by the Coulomb barrier, and neutron emission dominates the particle decay channels. In neutron-decay experiments of giant resonances in ^{208}Pb an excess of neutron emission was found with respect to the statistical-model calculations in the case of the ISGMR, whereas the decay of the ISGQR seemed to proceed fully via the statistical component [4–6].

In addition to the interest of studying isoscalar giant resonances in particle-decay experiments a systematic investigation of compression modes [ISGMR and isoscalar giant dipole resonance (ISGDR)] was pursued in connection with the experimental determination of the nuclear incompressibility due to its direct relationship with the excitation energy of these resonances [10–13]. Singles experiments using inelastic α -scattering were continuously developed to deduce more

*Electronic address: hunyadi@atomki.hu; Present address: Institute of Nuclear Research of the Hungarian Academy of Sciences, H-4001 Debrecen, Hungary.

†Present address: TRIUMF, 4004 Wesbrook Mall, Vancouver BC, V6T 2A3, Canada.

precise values of the incompressibility [14–24]. This was motivated by the need for a more reliable application of the nuclear equation of state, e.g., in model calculations of various astrophysical processes or in descriptions of heavy-ion reactions. Intensive experimental efforts were devoted to the detailed investigations of the ISGMR in the past two decades following its discovery in 1977 [25,26]. The first unambiguous evidence for the existence of the ISGDR was reported only in 1997 [18]. The difficulties were caused mainly by the relatively weak excitation of the $3\hbar\omega$ ISGDR, which in addition was distributed with a relatively large width superimposed on an overwhelming nuclear continuum and instrumental background. Moreover, a partial overlap with the $3\hbar\omega$ high-energy octupole resonance (HEOR) further increased the uncertainties. Consequently, very little is known about the ISGDR and its microscopic structure. The only experimental result on its proton-decay properties in ^{208}Pb was first reported in Refs. [27,28].

In the past few years, a series of singles experiments aimed at drawing a consistent picture of the ISGDR systematics using multipole-decomposition analysis (MDA) to define strength distributions in a wide excitation-energy range (10–35 MeV) [19–24]. However, the problem of separating the nuclear-background components from resonance strengths still remained due to the unknown multipole contents of the nuclear continuum. This MDA technique requires high-precision measurements in a wide angular region to decompose the spectra confidently into the different components, which then should have also a different angular distribution over the range measured. However, the results strongly depend on the model assumptions. Alternatively, the pronounced changes and large differences in the shapes of the angular distributions at very forward angles can also be exploited, and various multipolarities (especially $L \leq 2$) can easily be disentangled in a less model-dependent way [4,18]. However, measurements close to 0° often suffer from a substantial contribution of instrumental background in addition to the nuclear continuum of nonresonant processes of quasifree scattering and various pick-up/break-up reactions. The elimination of the background components was the major difficulty in the singles experiments, and the choice of the background-subtraction technique resulted in large uncertainties that added to the statistical error of giant-resonance parameters.

The theoretical angular distributions for a number of multipolarities ($L \leq 3$) illustrating these differences in shapes were calculated in the distorted-wave Born approximation (DWBA) using the code CHUCK [32]. The parameters of the optical-model potentials used in the DWBA calculations are listed in Table I for all three nuclei. The calculated angular distributions are shown in Fig. 1. The magnitudes of the angular distributions are determined for giant-resonance modes with the given multipolarities with the assumption of 100% exhaustion of the EWSR at the centroid energies listed in Table II, which were taken from the literature [22–24,33]. The implicit-folding model as described in Ref. [1] was used to determine the deformation parameters for a 100% exhaustion of the EWSR.

In addition to the main experimental goal of our decay measurements on studying direct-decay properties and micro-

TABLE I. Parameters of the optical-model potentials used in the DWBA calculations of the inelastic-scattering cross sections for the various isoscalar giant resonances in ^{90}Zr , ^{116}Sn , and ^{208}Pb .

Nucleus	V (MeV)	r_V (fm)	a_V (fm)	W (MeV)	r_W (fm)	a_W (fm)	r_C (fm)
$^{90}\text{Zr}1^a$	117.5	1.27	0.78	21.0	1.56	0.57	1.3
$^{116}\text{Sn}2^b$	121.5	1.21	0.84	21.9	1.51	0.63	1.3
$^{208}\text{Pb}3^c$	119.9	1.26	0.74	21.3	1.45	0.80	1.3

^aReference [29].

^bReference [30].

^cReference [31].

scopic structure of the ISGDR, it was important to overcome the problems connected with background subtraction based on the above-mentioned considerations to allow a better determination of the giant-resonance gross properties. Although a part of the instrumental background caused by reactions

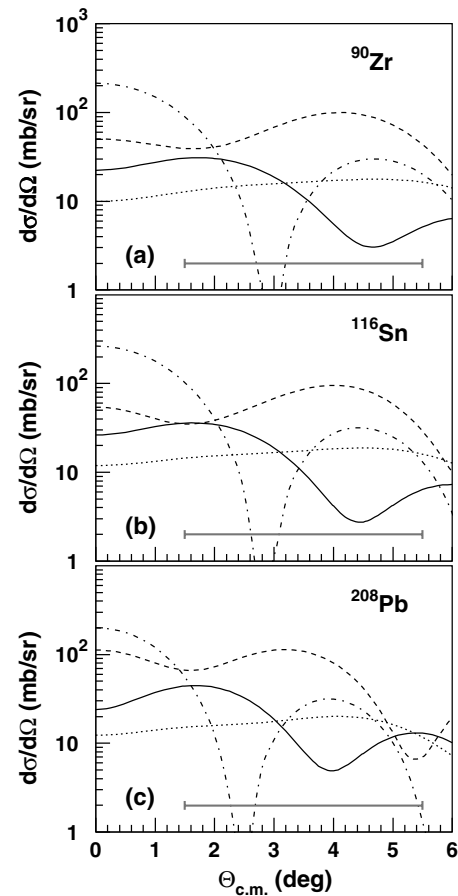


FIG. 1. Differential cross sections for exciting isoscalar giant resonances via the (α, α') reaction on various targets calculated in DWBA, assuming 100% exhaustion of the respective energy-weighted sum rules. The calculation was performed at $E_\alpha = 200$ MeV. The excitation energies of the resonances used in the calculations are listed in Table II. The curves drawn are for ISGMR (dash-dotted), ISGDR (solid), ISGQR (dashed), and HEOR (dotted). The region of angular acceptance in the present experiment is also indicated.

TABLE II. Centroid energies of isoscalar giant resonances with $L = 0-3$ obtained from the MD analysis of singles strength distributions, which were used in DWBA calculations of the differential cross sections.

L	0	1	2	3
^{90}Zr	16.6(0.1) ^a	26.9(0.7) ^a	14.65(0.20) ^b	26.5(1.5) ^c
^{116}Sn	15.4(0.1) ^a	25.4(0.5) ^a	13.50(0.35) ^d	23.3(0.8) ^d
^{208}Pb	13.4(0.2) ^a	22.7(0.2) ^a	10.89(0.30) ^d	19.6(0.5) ^d

^aReference [24].

^bReference [22].

^cReference [33].

^dReference [23].

in various elements of the beam line and the spectrometer could be removed by time-of-flight (TOF) measurements of the ejectiles, the major part is, in principle, suppressed by applying coincidence conditions. This is due to the fact that particles detected in the spectrometer, but that originate from scattering centers other than the target, are randomly correlated in time with particles detected with the coincidence detectors. Furthermore, the nuclear continuum is also expected to be suppressed by placing the coincidence detectors at backward angles, which filters out events associated with forward-peaked processes like quasifree scattering and pick-up/break-up reactions. The nuclear continuum of (α, α') scattering is still present in the true coincidence spectra. By gating on the particle direct-decay channels, which populate single-hole states in the daughter nuclei, contributions from excitations of more complex (np-nh) states are removed, and the direct decay from initial $1p-1h$ configurations is enhanced.

In this article, we provide a detailed description of our coincidence experiments for studying the direct neutron-decay properties of the $3\hbar\omega$ ISGDR in ^{90}Zr , ^{116}Sn , and ^{208}Pb . We aimed at extracting direct-decay branching ratios for the ISGDR and comparing them to the continuum-random-phase approximation (RPA) calculations in the framework of a semimicroscopic approach [34]. We also focus on resonances in the continuum region above the ISGDR, where $4\hbar\omega$ overtone modes of the ISGQR and ISGMR are expected. This was primarily motivated by experimental indications reported in the previous work on direct proton-decay measurements [27] and by the intensive efforts of continuum-RPA calculations to describe the main properties of such high-energy resonance modes [34].

II. EXPERIMENT

The experiments were performed at the AGOR superconducting cyclotron facility at KVI, which provided an α -particle beam with energy of 200 MeV. The α -beam bombarded ^{90}Zr , ^{116}Sn , and ^{208}Pb targets with enrichments $>97\%$ and with nominal thicknesses of 5.1, 5.0, and 3.5 mg/cm², respectively. The ejectiles were momentum analyzed by the Big-Bite Spectrometer (BBS) [35]. The BBS is equipped with a composite focal-plane detector system, which was developed in the framework of the EuroSuperNova (ESN) collaboration [36]. Measurements at very forward angles,

which were necessary to disentangle effectively the contributions of different multiplicities, required a very careful beam tuning to avoid disadvantageous scattering of beam-halo particles on the beam pipes, the entrance slit, and other internal elements of the spectrometer. As a necessary consequence, the use of a dispersion-matched beam was not possible, because it would have enhanced the rate of background events, and the compromise of moderate energy resolution had to be accepted. This had, however, minor influence on the final-state excitation energy resolution that was dominated by the neutron energy resolution. Further suppression of the instrumental background was achieved by removing the entrance slits of the spectrometer, which would have otherwise led to an increased rate of elastically scattered α particles at small angles that subsequently scatter off the slit edges.

The decay neutrons were observed in coincidence with the inelastically scattered α particles with the large-coverage detector array (EDEN) placed in the backward hemisphere with respect to the beam direction [37]. In the present setup the neutron-detector array consisted of 30 organic-liquid scintillators of type NE213 built for precise TOF measurements. The detectors were arranged symmetrically around the beam axis at a distance of 1.6 m from the target position. Each detector had a cylindrical geometry with a depth of 5 cm and a diameter of 20 cm. In this arrangement the 30 detectors covered a solid angle of 2.9% of 4π (364 msr).

There were two major concerns, which influenced the precision of neutron detection. Various sources of the background events had to be identified and suppressed as much as possible to reduce statistical errors. The contributions of neutrons originating from the beam pipe and the Faraday cup were suppressed by building a composite shield surrounding the neutron detectors, which consisted of lead and paraffin blocks for trapping both fast and thermal neutrons. Another source of background was caused by the high flux of γ rays from the target, to which the EDEN detectors were also sensitive. A complete separation of events caused by γ rays and neutrons could be achieved since liquid scintillators allow the use of pulse-shape discrimination (PSD) due to the different decay times of light signals induced by particles with different ionization mechanisms in the scintillator material. The PSD was performed by integrating the anode signals of the photomultipliers with charge-to-digital converters using charge-integration gates over short (30 ns) and long (400 ns) time intervals. The ratio of these integrated charges (PSD signal) carried the information on the type of the detected particles, and the distinction between the γ rays and neutrons could be performed on an event-by-event basis.

In Fig. 2(a), a two-dimensional plot of the PSD signal versus the TOF signal is shown, which demonstrates a clear separation between γ rays and neutrons along the vertical axis. The TOF of the neutrons was measured with respect to the radio frequency signal of the cyclotron. The prompt γ peak was used to determine the reference time for the TOF measurement. The TOF spectrum for prompt neutron events shown in Fig. 2(b) displayed a broad structure ranging between 30 and 170 ns relative to the prompt γ peak, which covered approximately four beam bursts with a beam repetition period of 30 ns.

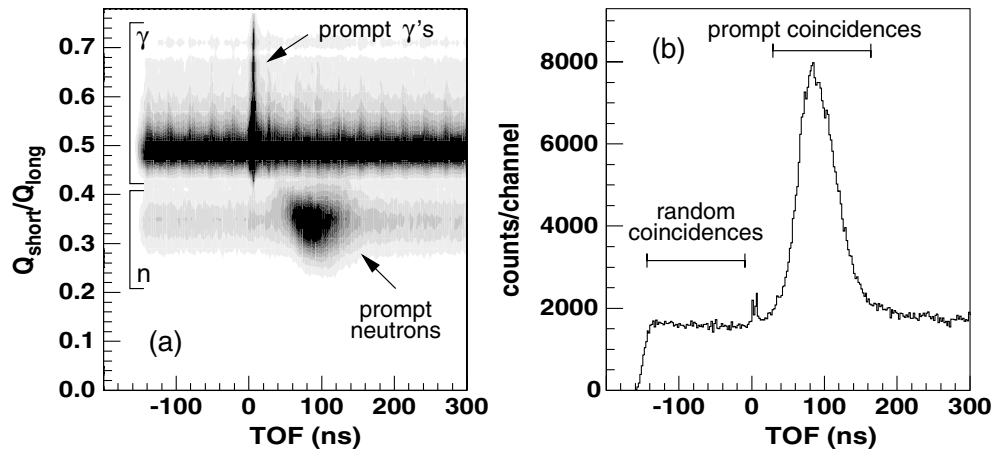


FIG. 2. (a) Two-dimensional plot of the PSD signal ($Q_{\text{short}}/Q_{\text{long}}$), calculated by dividing collected charges in the neutron detectors integrated over short (30 ns) and long (400 ns) time intervals, versus the time-of-flight of particles hitting the neutron detectors. Hits of γ rays (upper part) and neutron (lower part) are well separated according to the PSD signal. (b) The time-of-flight spectrum of neutrons selected by the PSD signal shown in panel (a). Regions of prompt and random coincidences selected in the analysis are also indicated.

The overall time resolution for the prompt γ -burst peak was 1.8 ns. This was determined mainly by the resolution of the signal-processing electronics (discriminators, time-digital converters), the time structure of the beam bursts, the response time of the photomultipliers, and the finite dimensions of the scintillator units. This time resolution of 1.8 ns corresponded to an energy resolution of 1.5–2 MeV for fast neutrons with a kinetic energy in the range of interest ($E_n = 12$ –16 MeV). The continuous background under the prompt structure shown in Fig. 2(b) was attributed to random coincidences. The prompt-to-random ratio of counts integrated under the prompt structure of neutron coincidences was approximately 2.

The combination of the BBS and the ESN focal-plane detector was an effective and well-suited tool to satisfy the requirements for particle identification, momentum analysis, and reconstruction of the scattering angle of the ejectiles [36]. The ESN detector was designed to measure the incident positions and angles of scattered particles by two two-dimensional vertical-drift chambers (VDC) covering the whole focal plane. In the present setup this allowed the observation of an excitation-energy range of 10–70 MeV due to the large momentum acceptance of the spectrometer; however, the protective shielding around the Faraday cup shadowed a part of the angular acceptance below 15 MeV, limiting the analysis of angular distributions. However, the total angular acceptance, which was determined by the entrance window of the spectrometer, covered a solid angle of 6 msr. This corresponded to an angular range of 1.5° – 5.5° in the laboratory frame, when the central axis of the spectrometer was set at 2.8° , which was found to be an optimal position for two reasons. First, the spectrometer covered the angles, at which the differential cross sections for inelastic dipole excitations exhibit their maximum and minimum values. Second, the entrance window minimized the number of scattered particles originating from the interior of the spectrometer. The asymmetric angular coverage around the central axis at 2.8° resulted

from a software cut of angles below 1.5° in the off-line analysis because of the overwhelming elastic-scattering yield there.

To measure the TOF of charged particles passing through the BBS, the focal-plane detector was equipped with two scintillator planes for providing accurate timing signals for the front-end electronics. The TOF information was also essential to filter out contributions of the instrumental background, especially due to particles from the Faraday cup and from neutron-induced reactions in the focal plane.

The scattering angles of the ejectiles were calculated from the incident angles at the focal plane, determined by the VDCs, using a ray-tracing algorithm, which is based on the one-to-one projection of the focal-plane and target coordinates. An angular resolution of approximately 0.5° was achieved and optimized in the excitation energy region of the ISGDR (20–30 MeV). This angular resolution was found sufficient to follow the variations of the calculated angular distributions and to disentangle the various multipole strengths.

The momentum and kinetic energy of the ejectiles was determined by using the position information from the front VDC with a trajectory reconstruction algorithm. Some of the ion-optical aberrations of the BBS and kinematical broadening were corrected for to improve the resolution of the measured spectra. The energy calibrations were performed by measuring inelastic α scattering from a ^{12}C target. An excitation energy resolution of ~ 350 keV was achieved, which is quite acceptable for observing gross structures of giant resonances in heavy nuclei, because their typical width is in the range of a few MeV. However, this resolution in combination with that of the decay neutrons in the direct-decay channels exceeded the average level spacing at low excitation energies in the daughter nuclei, which was obviously insufficient to resolve the individual neutron-hole states. Nevertheless, a good separation of the direct- and statistical-decay components was still possible, and integrated branching ratios for the direct-decay components could be deduced.

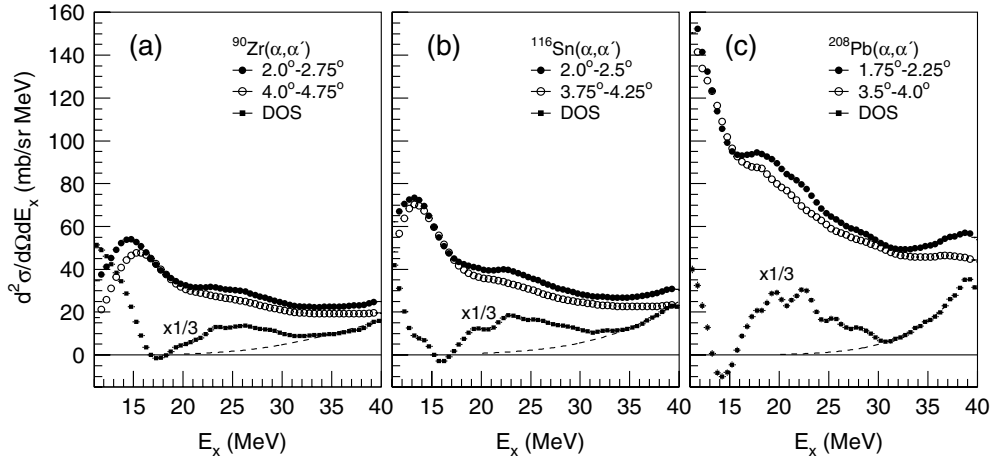


FIG. 3. Inelastic α -scattering spectra for angular regions, in which the ISGDR has a maximum (filled circles) and a minimum (open circles) differential cross section. The difference of these spectra (DOS) is also shown and magnified with a factor of 3 (filled squares). The dashed curves represent an assumed contribution of quasifree processes under the ISGDR structures.

III. EXPERIMENTAL RESULTS

A. Singles data

Singles spectra of inelastic α scattering were measured simultaneously with the coincidence spectra to obtain differential cross sections of the ISGDR for the determination of the branching ratios and exhaustion factors of the EWSR. In general, multipole strengths in inelastic-scattering spectra of inclusive measurements are evaluated with the multipole decomposition analysis (MDA), provided a sufficiently wide angular region is measured to apply an approximately orthogonal basis of calculated angular distributions in the fitting procedure. However, the MDA can effectively be employed for strongly excited resonance structures (e.g., ISGQR and ISGMR), where the relative contribution of the background is small, whereas weak resonances at higher excitation energies can be analyzed only with large statistical uncertainties and the resonance strengths cannot be separated from the continuum for a given multipolarity. This is mainly the consequence of the assumption that several multipolarities are present in the nuclear continuum and components of higher angular momenta ($L \geq 3$) possessing similar angular distributions are less confidently decomposed. In the alternative technique of the difference-of-spectra (DOS), this feature of angular distributions is exploited to separate multipolarities of high and low angular momenta. The angular acceptance of the spectrometer in the present experiments (1.5° – 5.5°) covered a region, in which the differential cross section for $L = 1$ has both a maximum and a local minimum (see Fig. 1). Contributions of multipole strengths, especially of the HEOR, overlapping in excitation energy with ISGDR had to be minimized by the appropriate choice of angular regions in the DOS procedure. The (α, α') spectra were generated at these angles and subtracted as shown in Fig. 3. The enhancement of the ISGDR is significant in the difference spectra around the centroid energies listed in Table II, whereas at lower excitation energies other multipole strengths (mainly $L = 0$ and $L = 2$) seem to cancel out, suggesting that angular regions for the

DOS were chosen appropriately. It must be noted that below 15 MeV a part of the angular acceptance was cut off, which led to an artifact deviation between the spectra of different angles. Nevertheless, it could be estimated from the DWBA calculations that some admixtures of other multipole strengths in the order of 10–25% of the integrated double-differential cross sections were still present in the difference spectra. In the case of optimally chosen angular regions the systematic error caused by these multipole admixtures can be kept below the statistical uncertainties, slightly affecting the deduced differential cross sections. Furthermore, the distortion of the resonance shapes was also investigated and was found to lead to a ~ 1 MeV shift upward or downward in the centroid energies, depending on the relative sign of the admixtures, but its influence on the resonance widths was negligible compared to the statistical errors.

It can also be seen in Fig. 3 that at excitation energies above the ISGDR region some $L = 1$ strength is still present, which can be attributed to the $L = 1$ component of the nuclear continuum excited through quasifree processes. The distribution of this continuum is approximated with a Gaussian shape centered above 40 MeV, which gives a good estimate for its low-energy tail extrapolating in the ISGDR region (dashed curves in Fig. 3). In the case of ^{208}Pb the quasifree continuum is farther apart from the ISGDR, which can be explained with its smaller resonance width and lower excitation energy.

In Fig. 4 the results of the DOS analysis for $L \leq 2$ are plotted for the three nuclei studied. Resonance structures of $L = 0$ and $L = 2$ multipolarities are clearly observed in the region of $2\hbar\omega$ (~ 14 MeV in ^{208}Pb), although weak, but significant $L = 1$ concentration is found in the region of $3\hbar\omega$ excitation energy (~ 21 MeV in ^{208}Pb), as discussed in the previous paragraph. As mainly the HEOR overlaps with the ISGDR in excitation energy (typically $E_{\text{ISGDR}} - E_{\text{HEOR}} = 1$ – 3 MeV), its contribution to the $L = 1$ difference spectra was calculated from the DWBA angular distributions. However, a substantial effect on the gross resonance parameters was not expected from the admixed $L = 3$ strength, which was

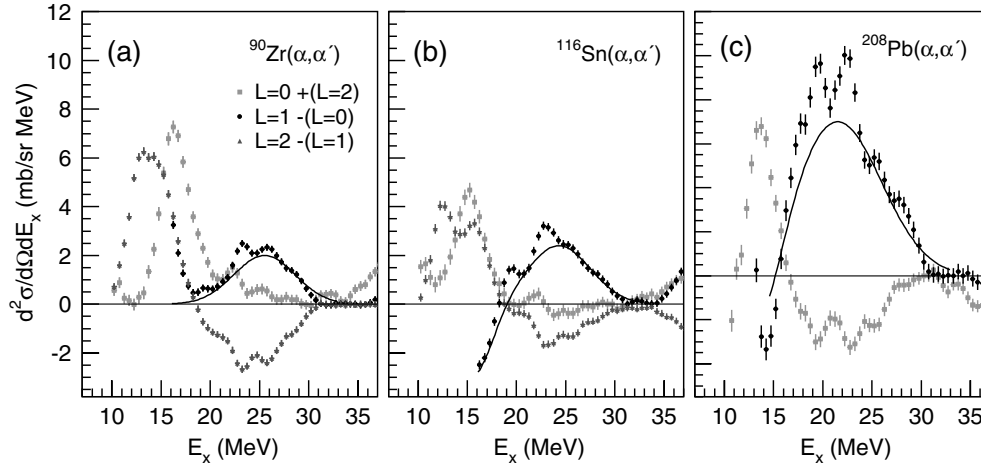


FIG. 4. Difference spectra in terms of double-differential cross sections from the singles measurements. The plots represent difference spectra selecting multiplicities with $L = 0, 1$, and 2 . Algebraic contributions of other multiplicities are given in brackets, which could not be eliminated by the difference-of-spectra procedure in the observed angular region. The curves represent the cross section for the (α, α') reaction composed of Gaussians for the ISGDR and the ISGMR (with opposite signs), excluding the superimposed structures due to the contaminant $^{16}\text{O}(\alpha, \alpha')$ reaction.

calculated to be 5–15% of the integrated double-differential cross sections in the ISGDR peak. In addition, for ^{90}Zr the increased resonance widths relative to the heavier nuclei may also lead to a partial overlap of the ISGMR in the low-energy side of the ISGDR, as can be seen in Fig. 4(a). Further appearance of $L = 0$ and $L = 2$ strengths in the $3\hbar\omega$ region is not expected; nevertheless small contributions of $L = 0$ and $L = 24\hbar\omega$ overtones to the ISGDR cannot be excluded as they are predicted to have relatively large width due to their stronger damping and less concentrated particle-hole structure. In Table III the centroid energies as m_1/m_0 ratio of momenta extracted for the ISGDR are listed and compared to literature data.

At lower excitation energies the determination of the ISGQR gross properties through the DOS analysis was hampered by the reduced angular acceptance below 15 MeV due to the protective shielding around the Faraday cup, as mentioned above. Especially in the case of ^{208}Pb , where the ISGQR is located at the lowest excitation energy in the three nuclei, the DOS analysis was not applicable.

In spite of the good statistics of the singles spectra large uncertainties stemmed from the unclear dependence of the instrumental background on the scattering angle and the focal-plane position, and from the nuclear continuum, to which mostly quasifree processes contribute. In addition, some oxygen contamination of the targets appeared as multiple structures superimposed on the (α, α') spectrum around 20 MeV, but at higher excitation energies no significant contributions were observed. These resonances of ^{16}O could be discriminated due to their relatively narrow structures and their contribution was excluded in the integration of the ISGDR structure, as indicated by solid curves in Fig. 4.

The differential cross sections for the ISGDR regions were obtained by the integration of the double-differential cross sections in the $L = 1$ difference spectra, excluding contributions of quasifree continuum and reactions on oxygen contamination of the target. The results are listed in Table IV and compared to the theoretical values from DWBA calculations. The uncertainties of the experimental cross sections come mainly from systematic errors assigned

TABLE III. m_1/m_0 centroid energies of the ISGDR obtained from the DOS analysis of the singles strength distributions and those gated on direct decay. For comparison, in the fourth column the result of our previous proton-decay experiment is given [27], and in the last column the most recent results of multipole-decomposition analyses (MDA) taken from the literature are given (see also Table II).

	Singles	n-decay	p-decay	Singles (MDA)	
	This work		Prev. work	Literature	
^{90}Zr	25.5(0.5)	25.1(0.5)		26.7(0.5) ^b	26.9(0.7) ^d
^{116}Sn	24.3(0.7)	24.7(0.4)		25.5(0.6) ^c	25.4(0.5) ^d
^{208}Pb	21.5(1.0)	21.2(0.7)	22.1(0.3) ^a	22.2(0.3) ^c	22.7(0.2) ^d

^aReference [27].

^bReference [22].

^cReference [23].

^dReference [24].

TABLE IV. Differential cross sections, exhaustions of the EWSR (H), and direct neutron-decay branching ratios (Br) obtained from the analysis of singles and coincidence data. The experimental and theoretical differential cross sections of giant-resonance structures identified in the singles DOS were compared. The theoretical values were calculated in DWBA assuming 100% exhaustion of the respective EWSR. The differential cross sections for the ISGDR in the direct-decay channel were determined by a simplified MDA, which assumed only $L = 1$ and $L = 3$ contributions. Branching ratios Br for the total direct-decay components were determined and compared to the results of continuum-RPA calculations summed for the decay channels populating the valence single-hole states.

Nucleus	L	DWBA $d\sigma/d\Omega_T$ (mb/sr)	Singles data		Direct-decay data		This work Br (%)	Theory ^a Br (%)
			$d\sigma/d\Omega$ (mb/sr)	H (%)	$d\sigma/d\Omega$ (mb/sr)	H (%)		
⁹⁰ Zr	0	26(11)	27.3(45)	106(47)				
	1	18(3)	16.5(20)	92(21)	0.8(1)	4.43(55)	4.8(9)	16.8
	2	34(9)	31.3(14)	93(24)				
¹¹⁶ Sn	0	22(11)	17.6(16)	79(41)				
	1	22.6(40)	20.7(15)	91(19)	1.05(12)	4.65(54)	5.1(7)	10.85
	2	27(8)	20.6(16)	77(24)				
²⁰⁸ Pb	0	15.7(56)	18.8(19)	119(45)				
	1	31.2(54)	38(5)	122(22)	4.0(3)	12.8(10)	10.5(16)	11.46
	2							

^aReference [34].

to the angular resolution ($\sim 0.5^\circ$), which affected the accuracy of defining angular ranges for the DOS procedure. This is especially crucial at angles where angular distributions have steep changes, like in the case of the ISGMR (see Fig. 1). The angular acceptance of the present experiments was optimized to study $L = 1$ multipolarity by covering both a maximum and a minimum of the differential cross sections, and the systematic error of the difference spectra were thus minimized for the ISGDR but not for other multipolarities.

In addition, differential cross sections of the calculated EWSR strengths also introduce systematic errors, which originate mainly from differences in the centroid energies of the giant resonances determined by various methods based either on energy-weighted moments or on assumptions of Gaussian shapes. As a result of the scatter in centroid energies and the steep decrease of cross sections per unit strength with increasing excitation energy, the relative errors of the respective EWSR's were typically 7, 11, and 4% for resonance modes with $L = 0, 1$, and 2 , respectively. Exhaustion factors of giant resonances with $L \leq 2$ were deduced as fractions of the EWSR, showing that most of the predicted strengths were observed in the resonance structures (see Table IV); however, the errors were found to be larger than those obtained from the MDA (e.g., [23]). The ISGDR structures were found to exhaust 92(21)%, 91(19)%, and 122(22)% of the EWSR for ⁹⁰Zr, ¹¹⁶Sn, and ²⁰⁸Pb, respectively, which are in satisfactory agreement with the latest experimental data [21,23], but are slightly underestimated by the results of continuum-RPA calculations [34].

B. Coincidence data

The analysis of the coincidence data was performed on the basis of the following requirements concerning the determination of the direct-decay branching ratios for the ISGDR:

(a) correction for random coincidences and elimination of γ -ray events based on the pulse-shape discrimination technique of the neutron detectors, (b) separation of the direct and statistical components of neutron decay by analyzing the shapes of the kinetic-energy spectra of emitted neutrons, (c) extraction of various giant-resonance strengths in terms of differential cross sections for different multipolarities (especially for $L = 1$) based on the analysis of angular-distribution measurements, and (d) calculation of the direct-decay branching ratios from the cross sections deduced for the coincidence and singles measurements and comparison to recent continuum-RPA results.

As a first step, various background components due to the instrumental scattering events and quasifree knock-out processes were eliminated in the coincidence spectra by correcting for random coincidences and by measuring the neutrons at backward angles, respectively. The background remaining in the coincidence spectra must be associated with inelastic scattering into the nuclear continuum. The discrimination between this continuum and the resonance strengths exploits the principal differences in their decay properties and their angular distributions. States of complex np-nh excitations can also decay by particle emission. This emission follows the statistical rules of particle evaporation and therefore sensitively depends on the centrifugal barrier (and Coulomb barrier for charged particles). Because of the centrifugal barrier a strong enhancement of s -wave decay is expected with respect to decay components with higher orbital angular momenta.

The final-state spectra were projected for a region, where most of the ISGDR strength is known from previous singles experiments to be concentrated, and for the continuum at higher excitation energies. The results are shown in Fig. 5, in which the kinetic energy is converted to excitation energy of the daughter nucleus (final-state energy $E_{f.s.}$) using the simple formula of energy balance: $E_{f.s.} = E_x - E_n - S_n - E_r$, where

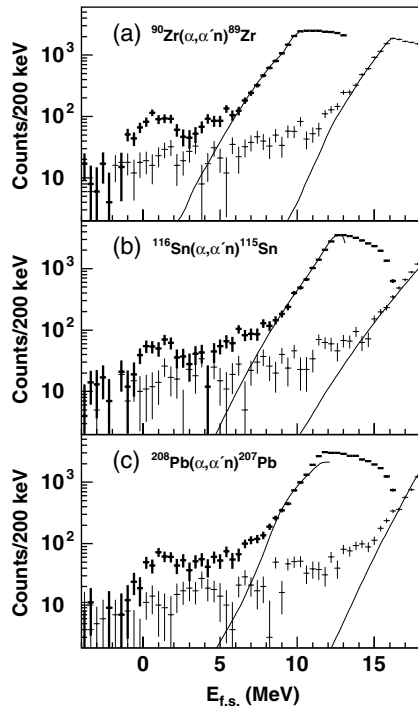


FIG. 5. Final-state spectra projected for events in the excitation energy region of the ISGDR (thick crosses) and of the continuum above (thin crosses). Statistical-decay calculations are represented by solid curves normalized to the experimental points. The excitation energy regions of the ISGDR and continuum were chosen to be 23–28 MeV (^{90}Zr), 22–27 MeV (^{116}Sn), 20–25 MeV (^{208}Pb) and 30–36 MeV (^{90}Zr), 29–35 MeV (^{116}Sn), 27–32 MeV (^{208}Pb), respectively.

the recoil energy E_r falls in the range of a few tens of keV and was negligible compared to the overall resolution. The spectra were compared to those of statistical decay calculations performed with the code CASCADE [38,39], which are also plotted in Fig. 5 over the experimental points. The steep shoulder of the statistical component was well reproduced by the calculation using a normalization to fit the experimental points with the requirement that calculated values should never exceed the experimental ones. Furthermore, statistical population of the low-lying single-hole states was found to be negligible in all three daughter nuclei. This is in contrast to the cases of low-lying giant resonances (ISGQR and ISGMR), where a predominant fraction of the hole-state population proceeds through statistical decay and the extraction of the relatively weak direct-decay component depends on assumptions of the statistical model, as was observed in the earlier experiments of Refs. [6,7].

In Fig. 5, the direct population of single-hole states from the ISGDR region appears as prominent structures in the spectra for all three nuclei, clearly separated from the statistical components. However, the energy resolution of ~ 1500 keV, stemming from the less accurate TOF measurement of faster neutrons, was insufficient to resolve the individual low-lying neutron-hole states and to extract partial branching ratios. It is worth noting that the population of single-hole states from decay of the ISGDR region is still more pronounced compared to that of the continuum at higher excitation energy.

We assumed that the decay properties of the continuum—in general—should not change drastically between the ISGDR and continuum regions, and therefore any excess of neutron decay populating single-hole states must be associated with particle-hole strengths of giant resonances. However, it will be difficult to recognize any enhancement in the population of the low-lying states from the nuclear continuum because of the worsening resolution of faster neutrons emitted from higher excitation energies, where the continuum region was selected. For the ISGDR region the semidirect population of more complex final states in the energy range $E_{f.s.} = 3\text{--}6$ MeV was not so visible as that of the single-hole states, but for the continuum region a rather smooth distribution was observed from the sharply rising edge of statistical decay to the lowest hole states. The remarkable feature of the continuum is that a significant part of its decay could be attributed to nonstatistical decay, which may suggest the presence of other resonance strengths at excitation energies above the ISGDR. These could most likely be attributed to modes with higher multiplicities and/or overtone resonances.

The conversion of spectra to double-differential cross sections required first of all the analysis of the angular correlations between the decay neutrons and the residual nuclei. As a result, a rather constant angular correlation was observed for the direct-decay neutrons where all neutron detectors were placed at backward angles with $\Theta_n > 100^\circ$. This observed isotropy is possibly due to the averaging effect of the angular correlations for more decay branches to the unresolved final states and partly due to s -wave neutron decay when coupling to hole states favors such a decay for the giant resonances. This is in contrast to the steep increase expected at forward angles due to knock-out processes whose contribution to the true coincidence spectra becomes negligibly small when a coincidence with a neutron is required at backward angles.

The double-differential cross sections were obtained as function of the excitation energy for both the total and direct neutron-decay channels (Fig. 6). In Fig. 6(a) the coincidence spectra gated on the total neutron decay are dominated by the statistical decay channels, and their shapes are mostly determined by the increasing neutron multiplicity at high excitation energies. This fact makes the identification of giant resonances rather uncertain, since the reconstruction of spectra is strongly model-dependent due to the effect of neutron multiplicities. In Fig. 6(b) the direct decay events were selected in the region of $E_{f.s.} = 0\text{--}2.5$ MeV, in which the enhanced population of single-hole states was observed. However, at lower excitation energies, approaching the neutron separation thresholds, the single-hole states are more strongly populated, partly by statistical decay, because of the decreasing phase space for neutron decay. This can be seen by the sudden increase of cross sections with decreasing excitation energy. A major part of this statistical decay component, which may overlap with the ISGDR in excitation energy, can be disentangled from the direct-decay components based on the analysis of angular distributions as described below.

The part of the direct-decay population associated with $L = 1$ strength in the ISGDR region was determined on basis of the analysis of angular distributions. It is assumed

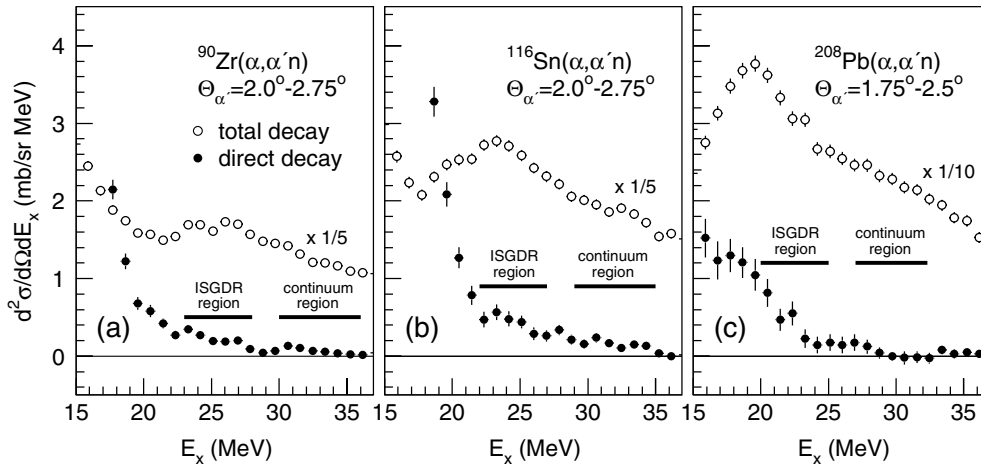


FIG. 6. Coincidence spectra projected for the total neutron-decay (empty circles) and direct neutron-decay channels defined by $E_{f.s.} = 0\text{--}2.5$ MeV (filled circles). The spectra gated on the total neutron-decay are downscaled by factors given in the panels. The regions selected to cover the ISGDR and the continuum at higher excitation energies are also indicated.

that from such a high excitation energy region only giant resonances decay to low-lying valence-hole states, therefore only $L = 3$ multipolarity of the HEOR must be disentangled from the ISGDR. Following a simplified procedure of MDA with only $L = 1$ and $L = 3$ components, differential cross sections and branching ratios can be more accurately extracted than those from the DOS analysis. Because the shapes of the angular distributions of higher multiplicities, including $L = 3$, exhibit rather flat behavior as function of angle, replacing all of them with a flat distribution in the measured angular range did not result in significant changes in the multipole decomposition of direct-decay cross sections. This also means that multipole components with $L \geq 3$ cannot be decomposed.

It was concluded from previous neutron-decay studies on the ISGMR [4] that multiplicities with $L \geq 4$ were admixed in the resonance region, because direct population of single-hole states with high angular momenta (e.g., the $13/2^+$ state in ^{207}Pb) was enhanced for the underlying continuum, whereas it was suppressed for the ISGMR. As discussed earlier, in the ISGDR region mainly the $3\hbar\omega$ octupole resonance (HEOR) overlaps with the ISGDR, but in the region of its high-energy tail weaker, $4\hbar\omega$ resonances are predicted, like the $L = 4$ hexadecapole resonance and overtone modes of the quadrupole and monopole resonances [34]. Indeed, this overlap of high-energy giant resonances is a direct consequence of their particle-hole structure consisting of couplings across distant nuclear shells and due to the large resonance widths in heavier nuclei as a result of mixing with the rather broadly distributed 2p-2h configurations.

The major advantage of this simplified MDA is the potential absence of low multiplicities of monopole and quadrupole strengths, especially in the center of the $3\hbar\omega$ region. The continuum region above the ISGDR was also analyzed in this fitting procedure assuming the presence of giant resonance strengths with $L = 0, 1$, and 2. However, a deep, well-defined minimum of χ^2 was found only with a fit of $L = 1$ and 2 multiplicities. The results of the fits are shown in Fig. 7 selecting the pronounced bump of the low-lying states in the

final-state spectra with $E_{f.s.} \leq 2.5$ MeV. It was found that the direct decay of the continuum region in ^{90}Zr and ^{116}Sn can be associated with a mixed multipole strengths of $L = 1$ and 2, but for ^{208}Pb the best fit was obtained for a pure $L = 2$ distribution. This observation is confirmed by the result of our previous experiment on the direct proton-decay studies [27], where a significant enhancement of $L = 2$ double-differential cross section was found centered at $E_x = 26.9 \pm 0.7$ MeV. Based on the continuum-RPA calculation of Ref. [34], which predicts the overtone mode of the ISGQR (denoted ISGQR2) in ^{208}Pb at $E_x = 30.5$ MeV, the present observation of the $L = 2$ strength in this excitation energy region may be assigned to this resonance mode. The poor statistics of the direct-decay channels from the continuum region did not allow either to find evidence for the presence of other predicted resonance modes like the $4\hbar\omega$ ISGMR2 in the analysis of angular distributions, nor to extract strength distributions as a function of the excitation energy similarly to our proton-decay studies.

As the enhanced bumps around the ground state of daughter nuclei up to $E_{f.s.} = 2.5$ MeV may contain states with complex structures, which is especially true for ^{89}Zr and ^{115}Sn , where valence neutron-hole states are located below 1.5 and 1 MeV, respectively (see Table V), the $L = 1$ component of the ISGDR

TABLE V. Valence neutron-hole states of the daughter nuclei included for summing partial branching ratios of continuum-RPA calculations [34].

^{89}Zr		^{115}Sn		^{207}Pb	
E_x (MeV)	lj	E_x (MeV)	lj	E_x (MeV)	lj
0.000	$g_{9/2}$	0.000	$s_{1/2}$	0.000	$p_{1/2}$
0.588	$p_{1/2}$	0.497	$d_{3/2}$	0.570	$f_{5/2}$
1.095	$p_{3/2}$	0.613	$g_{7/2}$	0.898	$p_{3/2}$
1.451	$f_{5/2}$	0.713	$h_{11/2}$	1.633	$i_{13/2}$
		0.987	$d_{5/2}$	2.340	$f_{7/2}$

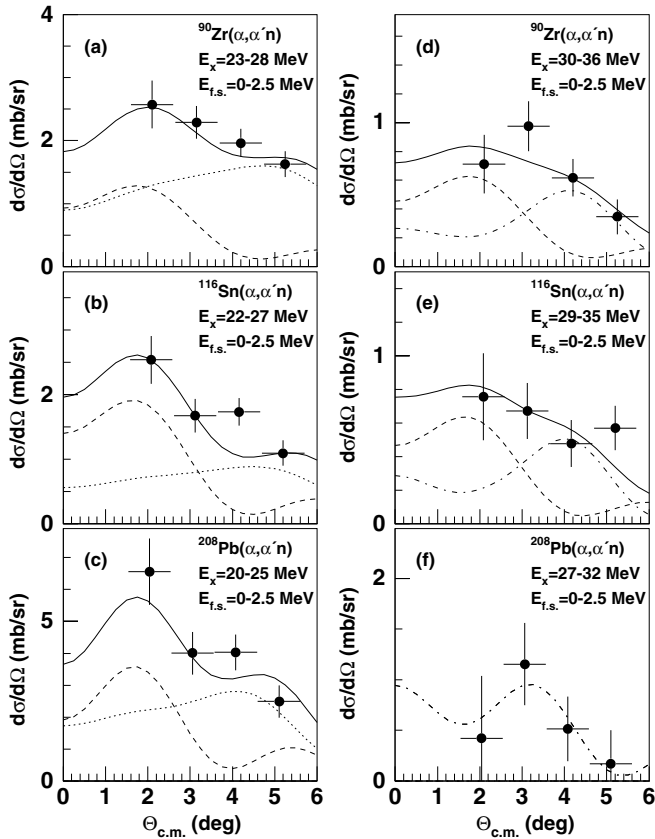


FIG. 7. Angular distributions in terms of differential cross sections for the ISGDR (left panels) and continuum (right panels) regions. The experimental points were fitted with angular distributions of the DWBA calculations for multipolarities, which are expected to be present in the given excitation energy regions: $L = 1$ (dashed) and $L = 3$ (dotted) for the ISGDR region; $L = 1$ (dashed) and $L = 2$ (dashed-dotted) for the continuum region.

region connected to the decay to these states must be analyzed as a function of the final-state energy. To correctly deduce differential cross sections and branching ratios for the ISGDR, a reliable separation of the single-hole state population is required for the $L = 1$ strength. The result of this analysis is shown in Fig. 8. A distinct structure was found for the decay of $L = 1$ multipolarity to the region of single-hole states for ^{207}Pb , but for ^{89}Zr and ^{115}Sn these structures were less pronounced, and in addition it was shifted to around $E_{f.s.} = 2$ MeV in ^{115}Sn , which may be understood as a consequence of the open neutron shell and the coupling to low-lying states. This observation suggests that semidirect population of low-lying complex (hole \otimes phonon) states via $L = 1$ strength is negligibly small. Thus, the differential cross sections and branching ratios can be determined neglecting the contribution of any of these states, except for ^{116}Sn . Concerning the low relative magnitude of the $L = 1$ component in the direct decay to ^{89}Zr , the HEOR and the continuum of higher multipolarities more likely populate single-hole states from the $3\hbar\omega$ region than the ISGDR. In the case of ^{207}Pb , the high relative magnitude of the $L = 1$ component suggested that in

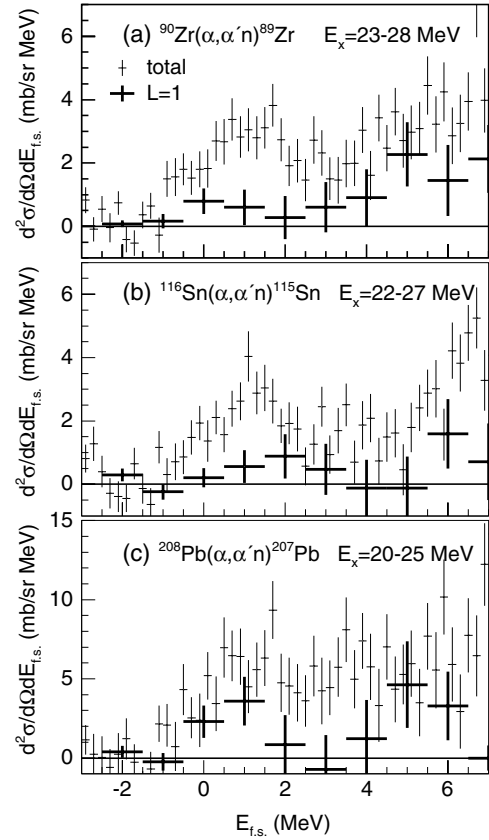


FIG. 8. Double-differential cross sections as a function of final-state energy projected from the ISGDR regions for all neutron-decay events (thin crosses) and selected for $L = 1$ strengths (thick crosses) determined by the analysis of angular distributions.

the direct-decay channels the ISGDR dominates the HEOR and the continuum.

The branching ratios are listed in Table IV and compared to the results of the continuum-RPA calculations from Ref. [34]. Because the single-hole states could not be resolved due to the insufficient energy resolution, the theoretical partial branching ratios had to be summed up for the valence neutron-hole states listed in Table V to compare with the experimental values. However, the experimental values of differential cross sections had to be corrected for the incomplete coverage of the total strength distributions by the selection of excitation energy regions of 23–28 MeV, 22–27 MeV, and 20–25 MeV for ^{90}Zr , ^{116}Sn , and ^{208}Pb , respectively. This was necessary because differential cross sections of ISGDR in the singles spectra were determined approximately for the whole resonance strength, whereas those of the direct-decay spectra were determined only for a part of it to exclude contributions from tails of other resonances as the ISGMR or probably the $4\hbar\omega$ ISGQR2. This correction was performed assuming a Gaussian or a Lorentzian shape for the ISGDR with an average width of 7(2), 6(2), and 4.0(15) MeV for the ^{90}Zr , ^{116}Sn , and ^{208}Pb , respectively, which were derived by taking several experimental and theoretical values from Refs. [18,23,27,34]. Correction factors were calculated from the ratio of integrals of the total resonance shape and the part in the selected excitation-energy region.

In the calculation of the theoretical branching ratios a common spectroscopic factor of $S = 1$ (for ^{115}Sn calculated v^2 was used) was applied, except for states, for which experimental data were available. In the case of ^{207}Pb , spectroscopic factors of 0.91 and 0.7 were taken for the $13/2^+$ and $7/2^-$ states from Ref. [40], respectively. In the case of ^{89}Zr , spectroscopic factors of 0.91, 1.2, 0.56, and 0.7 were taken for the $9/2^+$, $1/2^-$, $3/2^-$, and $5/2^-$ states from Ref. [41], respectively.

As a result, the experimental branching ratios of the ISGDR showed an excellent agreement for ^{208}Pb , whereas for ^{90}Zr and ^{116}Sn those were found significantly lower than predicted theoretically. In the case of ^{116}Sn , the deviation of a factor of ≈ 2 can partly be explained by an overestimation of the calculations, because experimental values of the spectroscopic factors for the single-hole states in question are typically 50–60% of the single-particle limit. In the case of ^{90}Zr , this argument cannot account for the large deficiency of single-hole-state population in the experiment, where a factor of 3.5 was found with respect to the calculations. This disagreement cannot be explained on the basis of the present theoretical descriptions. To understand these observations, it must also be considered that differences in the particle-hole coupling schemes of the ISGDR should be pursued by further experimental investigations, including the population of single-hole states in pf -shell nuclei. This would perhaps encourage those pursuing ISGDR studies to measure partial proton-decay branching ratios in Zr and Sn isotopes, and neutron-decay branching ratios in $N = 40$ isotones, where low-lying final states in the pf shell have a single-hole structure.

In summary, we have investigated the direct neutron-decay channels of the ISGDR in ^{90}Zr , ^{116}Sn , and ^{208}Pb by observing the population of low-lying, single neutron-hole states in the respective daughter nuclei. The decay properties of the ISGDR and a continuum region above the ISGDR were studied, and direct-decay branching ratios were determined. The use of the coincidence technique helped to suppress various background components, especially the instrumental background because it can generate only random coincidences. Furthermore, by measuring neutrons at backward angles in coincidence

with inelastically scattered α particles, the contribution of quasifree processes to the nuclear continuum was effectively eliminated.

The decay of the continuum region above the ISGDR did not show significant population of the single-hole states; however, the presence of resonance strengths could not be excluded, because the reduced resolution of neutron energies at higher excitation energy can smear out enhancements in decay structures. However, the analysis of angular distributions for the continuum region associated with the decay to low-lying states indicated the presence of $L = 2$ strength. In the case of ^{208}Pb , this may be associated with the $4\hbar\omega$ overtone of the ISGQR.

The extracted branching ratios of the ISGDR were compared to the predictions of the continuum-RPA calculations, which for ^{208}Pb yielded an excellent agreement, but for ^{90}Zr and ^{116}Sn the agreement was much less satisfactory. An appropriate refinement of the calculations is needed to resolve this deviation.

ACKNOWLEDGMENTS

We thank M. Urin for the interesting and helpful discussions. We acknowledge the support of the Marie Curie Actions programs of the European Commission under contracts HPMF-CT-2000-00663 and MERG-CT-2004-006379 and transnational access program under contract HPRI-CT-1999-00109. This work was performed as part of the research program of the Dutch Stichting voor Fundamenteel Onderzoek der Materie (FOM) with financial support from the Nederlandse Organisatie voor Wetenschappelijk Onderzoek (NWO). The Hungarian coauthors acknowledge the Hungarian fund OTKA under contracts N32570, D34587, and NK69035. U. Garg acknowledges a grant from the U.S. National Science Foundation (number PHY-0140324). B. Davids acknowledges support from the Natural Sciences and Engineering Research Council of Canada. M. Hunyadi acknowledges a grant from the János Bolyai Research Fellowship of the Hungarian Academy of Sciences.

-
- [1] M. N. Harakeh and A. van der Woude (2001), *Giant Resonances: Fundamental High-Frequency Modes of Nuclear Excitations* (Oxford University Press, New York, 2001), and reference therein.
- [2] W. Eylich, K. Fuchs, A. Hofmann, U. Scheib, H. Steuer, and H. Rebel, Phys. Rev. C **29**, 418 (1984).
- [3] K. Fuchs, W. Eylich, A. Hofmann, B. Mühldorfer, U. Scheib, H. Schlösser, and H. Rebel, Phys. Rev. C **32**, 418 (1985).
- [4] S. Brandenburg *et al.*, Nucl. Phys. **A466**, 29 (1987).
- [5] A. Bracco, J. R. Beene, N. Van Giai, P. F. Bortignon, F. Zardi, and R. A. Broglia, Phys. Rev. Lett. **60**, 2603 (1988).
- [6] S. Brandenburg, W. T. A. Borghols, A. G. Drentje, A. van der Woude, M. N. Harakeh, L. P. Ekström, A. Håkanson, L. Nilsson, N. Olsson, and R. De Leo, Phys. Rev. C **39**, 2448 (1989).
- [7] W. T. A. Borghols *et al.*, Nucl. Phys. **A504**, 231 (1989).
- [8] P. Grabmayr, G. J. Wagner, K. T. Knöpfle, H. Riedesel, P. Bogucki, J. D. Bronson, Y. W. Lui, U. Garg, and D. H. Youngblood, Phys. Rev. C **34**, 322 (1986).
- [9] Y. Toba, Y.-W. Lui, D. H. Youngblood, U. Garg, P. Grabmayr, K. T. Knöpfle, H. Riedesel, and G. J. Wagner, Phys. Rev. C **41**, 1417 (1990).
- [10] M. N. Harakeh and A. E. L. Dieperink, Phys. Rev. C **23**, 2329 (1981).
- [11] S. Stringari, Phys. Lett. **B108**, 232 (1982).
- [12] G. Colò, N. Van Giai, P. F. Bortignon, and M. R. Quaglia, Phys. Lett. **B485**, 362 (2000).
- [13] S. Shlomo and A. I. Sanzhur, Phys. Rev. C **65**, 044310 (2002).
- [14] C. Djalali, N. Marty, M. Morlet, and A. Willis, Nucl. Phys. **A380**, 42 (1982).
- [15] H. P. Morsch, M. Rogge, P. Turek, and C. Mayer-Böricke, Phys. Rev. Lett. **45**, 337 (1980).
- [16] H. P. Morsch, P. Decowski, M. Rogge, P. Turek, L. Zemło, S. A. Martin, G. P. A. Berg, W. Hürlimann, J. Meissburger, and J. G. M. Römer, Phys. Rev. C **28**, 1947 (1983).
- [17] G. S. Adams, T. A. Carey, J. B. McClelland, J. M. Moss, S. J. Seestrom-Morris, and D. Cook, Phys. Rev. C **33**, 2054 (1986).

- [18] B. F. Davis *et al.*, Phys. Rev. Lett. **79**, 609 (1997).
- [19] H. L. Clark, Y.-W. Lui, and D. H. Youngblood, Phys. Rev. C **63**, 031301(R) (2001).
- [20] M. Uchida *et al.*, Phys. Lett. **B557**, 12 (2003).
- [21] Y.-W. Lui, X. Chen, H. L. Clark, B. John, Y. Tokimoto, and D. H. Youngblood, Nucl. Phys. **A731**, 28c (2004).
- [22] D. H. Youngblood, Y.-W. Lui, B. John, Y. Tokimoto, H. L. Clark, and X. Chen, Phys. Rev. C **69**, 054312 (2004).
- [23] D. H. Youngblood, Y.-W. Lui, H. L. Clark, B. John, Y. Tokimoto, and X. Chen, Phys. Rev. C **69**, 034315 (2004).
- [24] M. Uchida *et al.*, Phys. Rev. C **69**, 051301(R) (2004).
- [25] M. N. Harakeh, K. van der Borg, T. Ishimatsu, H. P. Morsch, A. van der Woude, and F. E. Bertrand, Phys. Rev. Lett. **38**, 676 (1977).
- [26] D. H. Youngblood, C. M. Rozsa, J. M. Moss, D. R. Brown, and J. D. Bronson, Phys. Rev. Lett. **39**, 1188 (1977).
- [27] M. Hunyadi *et al.*, Phys. Lett. **B576**, 253 (2003).
- [28] M. Hunyadi *et al.*, Nucl. Phys. **A731**, 49c (2004).
- [29] D. A. Goldberg, S. M. Smith, and G. F. Burdzyk, Phys. Rev. C **10**, 1362 (1974).
- [30] L. Bimbot, B. Tatischeff, I. Brissaud, Y. Le Bornec, N. Frascaria, and A. Willis, Nucl. Phys. **A210**, 397 (1973).
- [31] T. Izumoto, Y. W. Lui, D. H. Youngblood, T. Udagawa, and T. Tamura, Phys. Rev. C **24**, 2179 (1981).
- [32] P. D. Kunz, Program CHUCK, University of Colorado (1983), unpublished.
- [33] T. Yamagata, S. Kishimoto, K. Yuasa, K. Iwamoto, B. Saeki, M. Tanaka, T. Fukuda, I. Miura, M. Inoue, and H. Ogata, Phys. Rev. C **23**, 937 (1981).
- [34] M. L. Gorelik, I. V. Safonov, and M. H. Urin, Phys. Rev. C **69**, 054322 (2004).
- [35] A. M. van den Berg, Nucl. Instrum. Methods B **99**, 637 (1995).
- [36] H. J. Wörtche, Nucl. Phys. **A687**, 321c (2001).
- [37] H. Laurent, H. Lefort, D. Beaumel, Y. Blumenfeld, S. Fortier, S. Galès, J. Guillot, J. C. Roynette, P. Volkov, and S. Brandenburg, Nucl. Instrum. Methods A **326**, 517 (1993).
- [38] F. Pühlhofer, Nucl. Phys. **A280**, 267 (1977).
- [39] M. N. Harakeh, Program CASCADE, extended version (1983).
- [40] C. A. Whitten, N. Stein, G. E. Holland, and D. A. Bromley, Phys. Rev. **188**, 1941 (1969).
- [41] G. Duhamel-Chrétien, G. Perrin, C. Perrin, V. Comparat, E. Gerlic, S. Galès, and C. P. Massolo, Phys. Rev. C **43**, 1116 (1991).